A versatile salt evaporation reactor system for SOFC *operando* studies on anode contamination and degradation with impedance spectroscopy

Gunnar Nurk[a], Peter Holtappels[a], Renato Figi[b], Jörg Wochele[c], Marco Wellinger[c], Artur Braun[a,*], Thomas Graule[a]

[a] *Laboratory for High Performance Ceramics, Empa, Swiss Federal Laboratories for Materials Science and Technology, Ueberlandstrasse 129, CH-8600 Dübendorf, Switzerland*
[b] *Laboratory for Analytical Chemistry, Empa, Swiss Federal Laboratories for Materials Science and Technology, CH-8600 Dübendorf, Switzerland*
[c] *Laboratory for Energy and Materials Cycles (LEM), Paul Scherrer Institut, CH-5232 Villigen PSI, Switzerland*

ARTICLE INFO

ABSTRACT

The dependence of the degradation kinetics in Ni–CGO (cerium–gadolinium oxide) solid oxide fuel cell (SOFC) anodes upon salt evaporation is demonstrated *operando* with a custom built versatile reactor system. The system is based on evaporation and subsequent condensation of low concentration salt vapor aerosol mixtures representative of salt vapors typically present in biomass gasification processes. Fast changes in the charge transfer and ohmic resistance are observed in the anodes fuelled with a gas mixture containing a high KCl vapor concentration. Rapid condensation of salt vapors into the porous anode and partial delamination of the anode from the electrolyte surface because of salt deposits inside the porous anode is observed. The flexibility to produce vapor–aerosol mixtures with different concentrations and particle size distributions is proved, and suitability of these aerosols for anode testing in long term fuel cell test is evaluated.

1. Introduction

The electrochemical conversion of biomass, which is obtained by the gasification of solid fuels such as wood, typically, achieves 25–30% electrical efficiency and 50% thermal efficiency in combustion engines or gas turbines. In an attractive combination with high temperature fuel cells, capable of direct conversion and of thermal integration of process steps like the gasification, an electrical efficiency of up to 50% is possible. Part of the released heat is available at utilizable temperature levels for cogeneration applications. It is a particular challenge to achieve these efficiencies in decentralized small scale applications (<1 MW), where biomass utilization could be a widespread application. The influence of wood-derived gasification gases on Ni–CGO anodes in intermediate temperature solid oxide fuel cells has been tested recently using simulated biofuel containing CO, CO_2, CH_4, and H_2 [1], where presence of 5 and 10% CH_4 caused carbon deposition and poor power output. The effect of impurities such as Na, Al, Si, and Cr arising from SOFC components such as insulating materials and gas supply tubes on the degradation and long term stability in a flatten tube type SOFC stack was tested with dry H_2 as fuel. In the course of 5000 h of operation, the ohmic resistance increased whereas the polarization resistance remained constant [2].

Gasified biomass is comparable with hot contaminated syngas (in contrast to "cold" biogas) containing high concentrations of CO/N_2 and numerous inorganic impurities, and thus may pose a serious challenge to fuel cell components (anode catalyst, fuel processing catalyst, and metal interconnects), particularly because the combustion chemistry of biomass fuel is more complex than the combustion chemistry of petroleum based fuels [3]. To tackle successfully problems which are related to gasified biomass utilization, it is necessary to understand the influence of different inorganic impurities on the performance of the SOFC anode.

One of the extensively studied catalyst-fuel impurity system is that of sulfur on metal surfaces like nickel because of its relevance for hydrodesulfurization [4] in the petrochemical industry. The detrimental effects of sulfur on Ni–cermet SOFC anodes, frequently referred to as *sulfur poisoning*, have been studied in numerous works focused on the aspects like the dependence of poisoning kinetics on the concentration of sulfur in fuel gas, influence of temperature [5], electrode polarization, current density [6] and microstructure of electrodes [7–9], and fuel chemical composition [10] on the poisoning kinetics, and the molecular structure of sulfur moieties present on SOFC anodes [11]. The motivation to use a coal-gas and gasified biomass as well as lignocellulosic ethanol as SOFC fuel to achieve higher utilization efficiencies have raised interest in the study of the influence of other inorganic impurities on the SOFC anode (elements such as As, P, Sb, Zn, Cl, Hg, Cd, Se, Si, etc.), some of which are scarcely documented, and some of which having aggressive influence on the SOFC infrastructure [12–14].

---

* Corresponding author. Tel.: +41 44 823 4850; fax: +41 44 823 4150.
  E-mail addresses: artur.braun@empa.ch, artur.braun@alumni.ethz.ch (A. Braun).

Elements gasified or volatilized in biomass or coal gasification may be present in various chemical forms (oxides, salts, carbonaceous compounds, hydroxides, etc.) depending on the feedstock and gasification processes [15]. The influence of impurities with higher activity such as S, P has been studied in different chemical forms in different molecular environments such as H_2S, S_2 [6] and PH_3 [16], P_4O_9 or P_4O_{10} [17] and in the same oxidation states but in different chemical compounds like H_2S, CH_3SH and COS [17,18]. Depending on chemical nature and environment, and poisoning mechanism, different chemical motifs of the same impurity may have different poisoning kinetics [17]. The oxidation state or molecular structure of impurities present in the gas depends on the substrates and the reaction conditions in the gasification process.

Biomass fuel differs from petroleum fuels, and so does their reaction chemistry [3]. Some of the inorganic elements present in gasified biomass come in the form of salts. Compared to most bituminous coals, one of the important features of biomass materials is the presence of considerable quantities of alkali and alkaline earth compounds (mainly K, Na, Mg and Ca) [19]. The influence of various inorganic salts in gasified biomass (NaCl, $NaCO_3$, KCl, KCO_3, K_2SO_4, ZnCl, etc.) on the SOFC anode performance and the influence of salt particle size on the anode degradation kinetics are not only not clear, but, to the best of our knowledge, have barely been addressed. However, it is certain that the chemical composition and particle size distribution of salt particles in gasified biomass or coal gas depend on the chemical composition of the feedstock, the reaction conditions of biomass gasification and also on the design of the gasifier equipment [20]. Usually, the concentration of impurities in fuel gas is observed and analyzed independently from the particle size distribution and impurity vapor pressure in the vapor–aerosol mixture in fuel gas. The kinetics and extent of condensation of salt vapors in the pores of the anode depends on the salt vapor pressure, on the topology of the pore space and on the salt properties. The concentration of the salt particles in the condensed phase and vapor phase results from the vapor pressure of the salt. To understand these processes in porous anodes and in gasified biomass atmosphere, and to apply the proper and most efficient purification method for cleaning these gases it is necessary to understand the influence of the chemical nature and the particle size of the salt on the behavior of a fuel cell anode.

We have therefore built a versatile and affordable reactor system to generate salt vapor–aerosol mixtures with different particle sizes for application in fuel cell studies, particularly as a pre-requisite for anode poisoning studies, which allows to *operando* record electrochemical impedance spectra under gas flow at high temperature. K and Cl are two major biomass impurities [21,22]. The concentration of Cl in biomass may be higher than in coal [19], and K contained in biomass is released into the gas phase as KCl [19, and references therein]. We have therefore selected KCl as the compound to use in this study, notwithstanding that studies on further impurities are important, such as Ca and Mg, or P.

2. Experimental

2.1. Design of the reactor system

The two principal components of the reactor system are the condensation interface and the test rig. The basic concept and design of the condensation interface is illustrated in Fig. 1.

Size and shape of the condensation interface are adapted to fit the tube furnace as sketched in Fig. 2. The central idea of our approach is to mix hot gases with salt vapors, which are formed in the furnace and quench them with cold gases to produce salt gas–aerosol mixtures, i.e. condensate salt vapors to bigger parti-
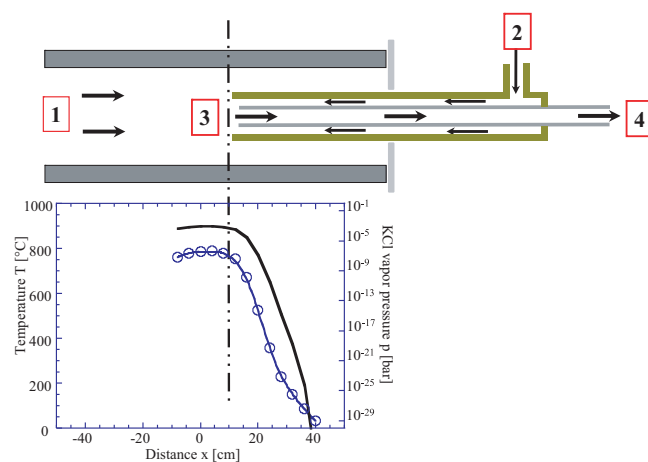

Fig. 1. Schematic sketch of the condensation interface and experimental temperature profile: (1) gas flow through the furnace (gases with salt vapors); (2) gas backflow (cold gas to initiate condensation of salt vapors); (3) approximate area where condensation of salt vapors takes place; (4) gas flow with salt–aerosol mixture; (T) temperature; (x) distance along tube furnace. Graph at bottom shows temperature (open symbols) and KCl vapor pressure (solid line) distribution across x.

cles. These aerosol particles can pass through colder tubes without condensation on the tube walls.

The condensation interface and the test rig are connected by a stainless steel gas line, which can be heated to 200 °C so as to avoid additional condensation of salt vapors prior to entering the test rig. Four photographs in Fig. 3 show give an overview of the apparatus. Fig. 3a shows the outlet of the ceramic tube furnace connected with an optional wash bottle to the test rig on the right side of the photo, as highlighted by Fig. 3b. A manifold of gas flow controllers and valves allows to mix the vapor with a variety of fuel gases, see the front panel in Fig. 3c. The test rig as such is cased in a metal housing with a volume of approximately 1 m^3. Here, another furnace encloses the ceramic bearings for the sample holder which provides the electric terminals for impedance spectroscopy measurements at high temperature with exposure to the fuel–vapor mixture in a fully computer controlled manner, see Fig. 3d.

2.2. Particle generation

The evaporation conditions in the test with KCl were 770 °C, corresponding to 3.9×10^{-4} bar partial pressure, and the gas flow through the furnace was varied from $10\,\text{ml min}^{-1} \le p_f \le 50\,\text{ml min}^{-1}$ and the gas backflow (cold gas for cooling the evaporated salt vapors) in the range from $0\,\text{ml min}^{-1} \le p_b \le 40\,\text{ml min}^{-1}$. The total gas flow was always kept $p_f + p_b = 50\,\text{ml min}^{-1}$, so as to have one more parameter fixed. The particle size dependence on the gas flow rates is demonstrated with a simple visual method by exposing a clean glass surface to the gas with salt particles and then measuring these particles by using an optical microscope (Fig. 4).
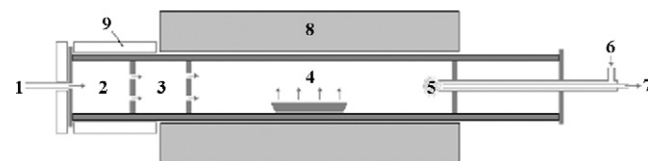

Fig. 2. Salt evaporation and condensation system: (1) gas flow to the furnace; (2 and 3) gas preheating chambers; (4) crucible with salt; (5) place where hot and cold gas will be mixed and condensation of salt vapor takes place; (6) cold gas flow to the condensation area; (7) gas stream with condensed salt particles; (8) furnace; (9) thermal insulation.
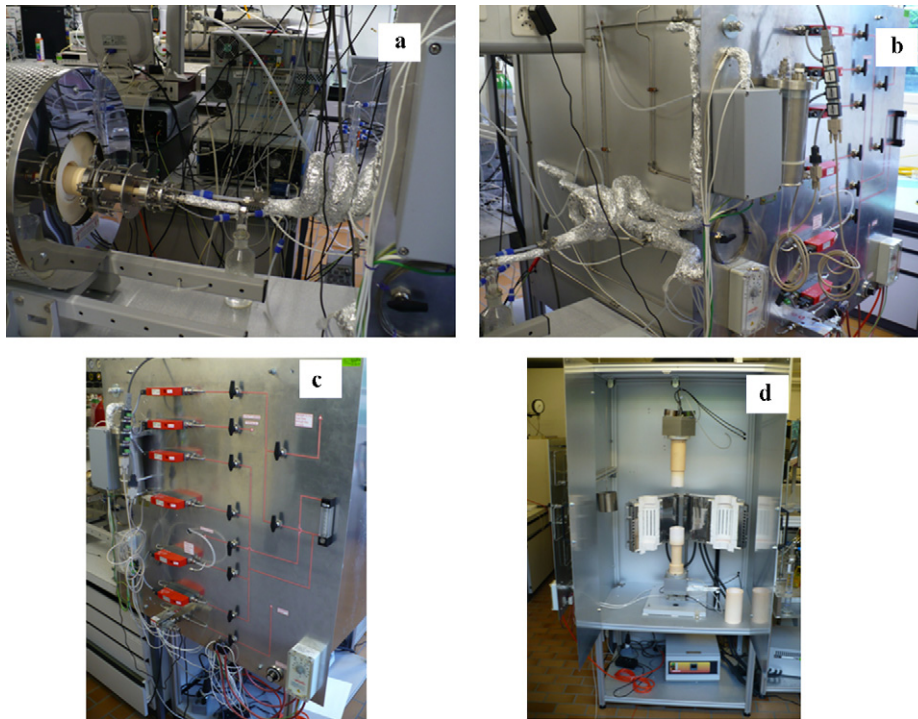
Fig. 3. Photographs of the evaporation reactor system: (a) furnace with evaporation system; (b) condensation interface; (c) front panel with gas mixing valves; (d) test rig with furnace and sample compartment and electric terminals for impedance spectroscopy measurements.

To determine the salt concentration, the gas was flushed through a series of three conventional gas-washing bottles. Salt concentrations in the gas-washing bottles decreased exponentially in the sequence of the bottles, as was measured by flame atomic absorption spectrometry (F-AAS). The salt concentration in the gas-washing bottle depends on the initial concentration of salt in the gas and on salt absorption coefficient in water as well as on factors connected with the gas-washing bottle design. Taking into account these factors, the initial salt concentration in the gas and salt absorption coefficient was calculated (see Appendix A). Based on these calculations, the initial KCl concentration in the gas mixture was 6 ppm. We cannot entirely rule out that a fraction of salt nanoparticles went through the gas-washing bottles without being dissolved in water and therefore the actual KCl concentration might be slightly underestimated. KCl and K_2SO_4 are dominant gas phase compounds during biomass combustion [23]. During biomass gasification, alkali and alkali earth compounds in the feedstock, may form sulfates and chlorides and cause heterogeneous nucleation and agglomeration in the gasifier. Alkali particles may exist in the fly ash or form aerosol particles in fuel gas [24]. The concentration of potassium in the raw fuel may vary from $0.4\,\mathrm{g\,kg^{-1}}$ to $7\,\mathrm{g\,kg^{-1}}$ [25]. Hot gas cleaning devices are able to reduce the alkali content by approx. 90% [26]. Taking into account these studies we can estimate that the KCl content varies from some ppm to several hundreds of ppms depending on the gasification conditions, raw materials and hot gas cleaning technologies. According to a recent thermodynamic equilibrium study, the K and Cl mole fractions in biomass gas may range from 4.4 ppm to 6.8 ppm, and from 88 ppm to 136 ppm, respectively, depending on whether the gasification is made using air or steam [21]. We are therefore confident that our experiment is representative to realistic SOFC operation conditions [22].

In the test with high salt concentration (HSC), the salt concentration in the gas was assumed to be approximately equal with equilibrium KCl vapor pressure at 900 °C because salt containers were placed in the same hot area of the furnace as the SOFC anode. No condensation of salt before arriving at the electrode was observed even at relatively low gas flows. The equilibrium vapor pressure of KCl at 900 °C is 3500 ppm.
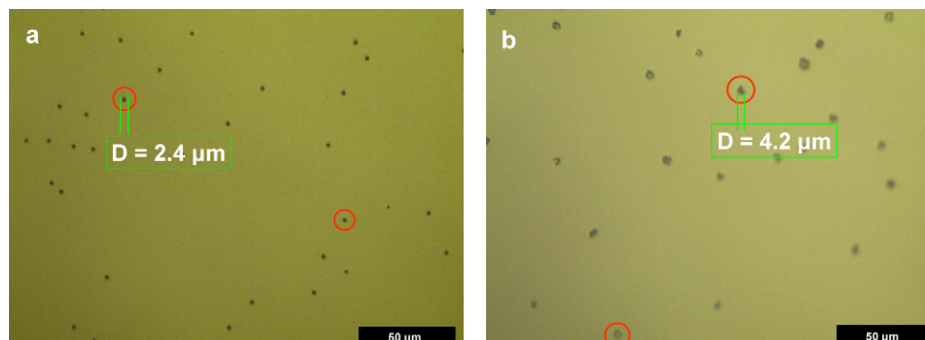

Fig. 4. Optical micrograph images showing KCl particles sticking to the glass surface in two different working regimes of the condensation interface: (a) $10\,\mathrm{ml\,min^{-1}}$ backflow (cold gas) and $40\,\mathrm{ml\,min^{-1}}$ main flow (gas with salt vapors), and (b) $40\,\mathrm{ml\,min^{-1}}$ backflow and $10\,\mathrm{ml\,min^{-1}}$ main flow.

2.3. Electrochemical impedance spectroscopy

Electrochemical impedance spectra were recorded on annular-shaped Ni–CGO (cerium gadolinium oxide) anodes (outer and inner diameters were 11 and 5 mm, respectively) supported on a 3YSZ (3 mol% yttria-stabilized zirconia) electrolyte pellet with 200 μm thickness. A La(Sr)MnO$_3$ cathode was screen printed as symmetrically as possible on the opposite side. Spring loaded Pt mesh current collectors and Au sealing gaskets were used to contact the electrodes and seal the anode compartment, respectively. The impedance spectra were recorded in a two electrode setup in the frequency range from 1 MHz to 0.1 Hz and in the potential range from 0.7 to OCV (Amel 7050 Potentsiostat, Quanteq 7200 Frequency Response Analyzer, software Junior Assist and Z-assist for data acquisition). Data were analyzed using ZView software from Scribner Associates Inc.

The measurements were performed in the following fuel gas mixture: 19.1% H$_2$, 78.1% N$_2$ and 2.4%H$_2$O. Gas flows were controlled with digital mass flow controllers (Vögtlin Instruments AG, Switzerland). Only high purity gases were used during the experiment (at least 99.995%). Stable and reproducible electrochemical behavior of single cells was observed during reproducibility tests.

Electron microscopy images were obtained with an environmental scanning electron microscope (FEI ESEM XL30 FEG). Energy dispersive X-ray spectra (EDAX) were obtained using a sapphire Si(Li) detector. The determination of salt particle sizes in fuel gas was carried out by a simple method in which particles from the gas stream have been collected on a flat glass surface by exposing the glass in gas flow for 15 min. The salt particles collected on the glass surface were measured with an optical microscope (DM 2500M).

3. Results and discussion

3.1. Principles of aerosol formation in the reactor system

The condensation interface is designed to simulate gasified biomass gas mixtures under realistic conditions. The basic idea of this set-up is based on the condensation effect that occurs, when gases saturated with salt vapors are cooled down by mixing with cold gas.

The aim of the condensation interface is to form nanoparticles from the evaporated salt, which are subsequently transported as aerosols to the test-rig; otherwise salt vapor condenses on tube walls and cold surfaces. For the production of the aerosols a well established method [27] has successfully been adopted and optimized [28] for the formation of ultra fine metal particles [29]. This principle of evaporation–condensation has also been adapted to transport gases containing heavy metal and alkali vapor from thermal treatment of solid fuel and waste [30] in thermo desorption spectrometry by connecting a furnace or a thermogravimeter to an inductively coupled plasma optical emission spectrometer [31,32]. The condensation interface was developed based on these ideas.

In these evaporation–condensation processes, metal or salt vapor is rapidly cooled (quenched) to form nano-particles. The particle formation proceeds via homogeneous nucleation of stable particles from condensable molecules (monomers), heterogeneous condensation of the remaining condensable monomers on the freshly nucleated, or on readily existing particles in the gas and growth of the particles by coagulation and agglomeration [33]. The parameters, which determine the particle size, are cooling rate, residence time, salt concentration and evaporation temperature [28].

Fast cooling rates are favorable for forming a large number of nuclei by homogeneous nucleation thereby reducing homogeneous condensation. A fast cooling rate is obtained by large temperature differences between the evaporation temperature and the

backflow gas and a high ratio of backflow gas to carrier gas. The residence time for cooling is influenced predominantly by the distance between the evaporation site and mixing zone and the carrier gas velocity. The concentration of the evaporated salt depends on the evaporation temperature, which in turn determines the vapor pressure, and the carrier gas flow. The evaporation temperature is in general kept constant in order to simulate a wood gas specific concentration.

The geometry of the setup (crucible position, furnace diameters and tubing, Figs. 2 and 3) is an important parameter set for proper aerosol formation and to prevent condensation on surfaces that would lead to losses. The backflow gas serves for cooling (quenching) and for diluting the carrier gas (sample gas, furnace gas). Both prevent further growth of particles. Rapid cooling serves for extensive nucleation. Dilution reduces the coagulation and growth of the nuclei by lowering the density of the nuclei (nano particles). Dilution reduces also the partial pressure of the salt and thereby increases the gaseous part of the salt.

It was demonstrated how the variation in particle diameter of the dominating fraction of salt particles present in the gas ranges from 0.5 to 4 μm and depends on gas flow rates. This is in reasonable agreement with realistic particle sizes present in gasified biomass [33]. It was demonstrated that by increasing the rate of gas backflow, i.e. the ratio of cold gas to hot gas in the condensation area, the salt vapors will be more condensed, and the average particle size will increase. This setup could be used in the case of different salts and gas flow rates. The total amount of salt in the gas can be regulated by the evaporation temperature, whereas the salt particle size is regulated by the gas flow rates of main and backflow.

3.2. SOFC anode electrochemical tests

To investigate the SOFC anode behavior under different salt vapor conditions, three different electrochemical tests as described in the previous chapter, were performed on nominally identical cells, denoted as reference test, high salt concentration (HSC) test (salt vapor concentration was approximately 3500 ppm of KCl) and low salt concentration (LSC) test performed using the condensation interface and carried out directly after a reference test on the same cell. The KCl concentration in the fuel gas mixture was approximately 6 ppm which is in the same range as the typical KCl concentration in woodgas [21,22].

During the reference test before salt supply the area specific resistance values (ASR) were measured at 900 °C. The reference test was performed for 190 h (approximately 7 days). The impedance of the cables measured at 900 °C was subtracted from the impedance data. The high frequency part should be characteristic for the resistance of the electrolyte but also contact resistances against current collector and electrodes, and contact against electrolyte and electrode. The area specific resistance (ASR) values in reference conditions were in the range from 1.87 to 1.97 Ω cm^2. The total charge transfer resistance R_{tot} averaged around 1.99 Ω cm^2 during the reference test. A stable ohmic resistance, but a small instability in the electrode resistance was observed. This was potentially caused by changes in the water content of the fuel gas because of fluctuations in the ambient conditions in the laboratory (Fig. 5).

3.2.1. Electrochemical test with high salt concentration

In the test with high salt concentration (HSC), the salt vapors were generated directly before the test rig in the same hot area of the furnace. The gases were not cooled between the location of salt evaporation and test rig and no unwanted condensation was detected on the test rig. The result of the anode durability test with high salt concentration is demonstrated by the impedance spectra in Fig. 6. The high frequency range of the impedance spectra should be characteristic to the electrolyte resistance but also contact resis-
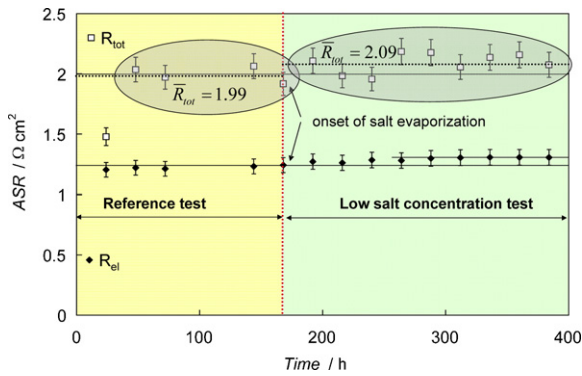
Fig. 5. Single cell total charge transfer resistance (R_{tot}) and high frequency ohmic resistance (R_{el}) dependence on time for Ni–CGO|3YSZ|LSMO system, without (first 190 h) and with low concentration KCl vapor–aerosol impurity (6 ppm) in the fuel gas mixture in 900 °C and 0.7 V.

Fig. 7. 3YSZ surface (dark grey) and Ni–CGO anode (light grey areas on the white surface) after the HSC test (3500 ppm of KCl) was finished. Delamination of anode pieces from the anode covered with salt (white part) and some cracks are visible.

tances against current collector and electrodes and contact against electrolyte and electrode. We observe a very fast increase in the charge transfer resistance as well as high frequency resistance. The ohmic resistance increased by approximately a factor of three, from 1.2 Ω cm² to 3.6 Ω cm², as read from the intercept with the Z'-axis and the charge transfer resistance from 0.61 Ω cm² to 2.11 Ω cm².

The increase in ohmic resistance can be caused by salt deposition on the interface between Pt current collector and anode top surface, or because of delamination of the anode as demonstrated in the micrograph in Fig. 7. The increase in charge transfer resistance is probably caused by delamination of the anode and possibly by the narrowing or blocking of pores because of condensation of salt vapors, and the consecutive gas diffusion limitations of fuel and reaction products. Fig. 8 shows an electron micrograph of the anode after exposure to high salt concentration. The circles indicate salt particles with a size of roughly 0.5 μm. The rectangles indicate needle like structures with a thickness of approximately 25 nm and a length of roughly 300 nm. A small decrease in the characteristic frequency of the impedance spectra is observed and most probably caused by the deposition of these salt particles in the porous anode structure, which may lead to gas diffusion limitations to the triple phase boundary and reaction products away from the electrode.

3.2.2. Electrochemical test with low salt concentration

We recall from Ref. [21] that the highest K and Cl concentrations were 88 ppm and 136 ppm, respectively. In response to the recent suggestion to test with higher concentrations of impurities [13], the HSC test with 3500 ppm Cl (Section 3.2.1) describes an extreme situation in the spirit of an "forced failure condition" and is not rep-
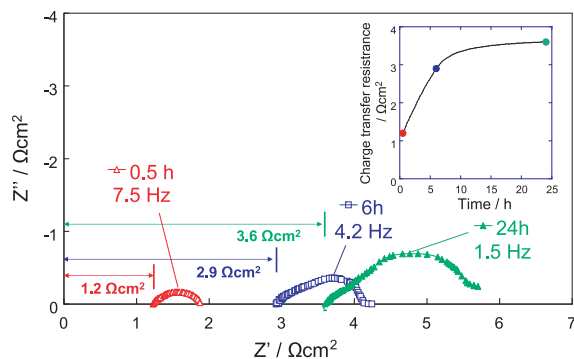
resentative of realistic working conditions in SOFC anodes fuelled with gasified biomass. To simulate salt vapors in gasified biomass gas mixtures with low salt concentration (LSC), the versatile "condensation interface" system setup (Fig. 2) was used.

The LSC test was carried out in excess of 200 h immediately after the reference test was finished. The fuel cell was kept under working conditions, i.e. at 0.7 V and 900 °C except for brief interruptions necessary for recording the impedance spectra. A low tendency towards increase in ohmic resistance as well as charge transfer resistance was observed (Fig. 5); i.e. while the reference test showed a total area specific resistance of averaged $R_{tot} = 1.99$ Ω cm², R_{tot} increased somewhat to averaged 2.09 Ω cm² during the LSC test. Following the electrochemical testing, microstructure analysis and elemental analysis of the porous anode with ESEM and EDX were carried out. Small salt residuals were observed on the anode surface. There were no – upon visual inspection – noticeable changes in the cermet microstructure, and only few small droplets of potassium chloride on the surface and inside the porous structure were detected. The EDX spectra were collected from the cross-section of the cell assembly at positions

Fig. 6. Nyquist plots for Ni–CGO|3YSZ|LSMO single cell after 0.5, 6 and 24 h (shown in figure) exposure in the fuel stream with high KCl concentration (approx. 3500 ppm) in 900 °C and 0.7 V. The inset shows the Faradaic resistance as a function of time.
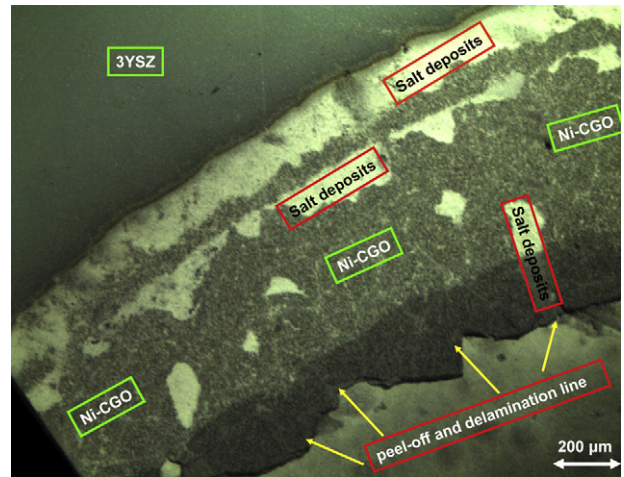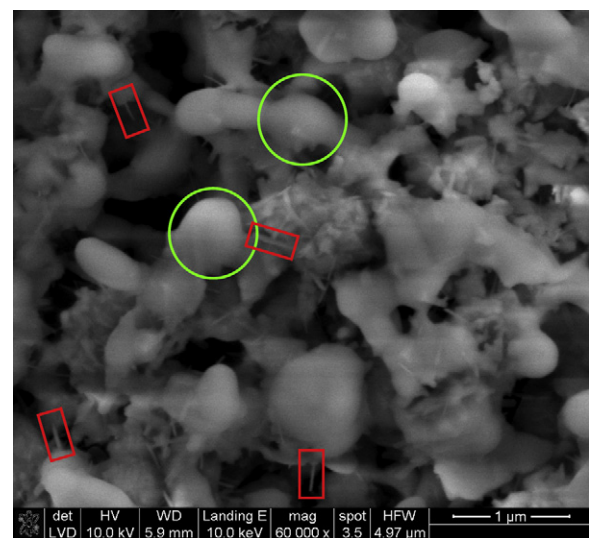

Fig. 8. Electron micrograph of the anode after exposure to the high salt concentration, showing white ice like deposits as indicated by the circles, and needle like structures as indicated by the rectangles.
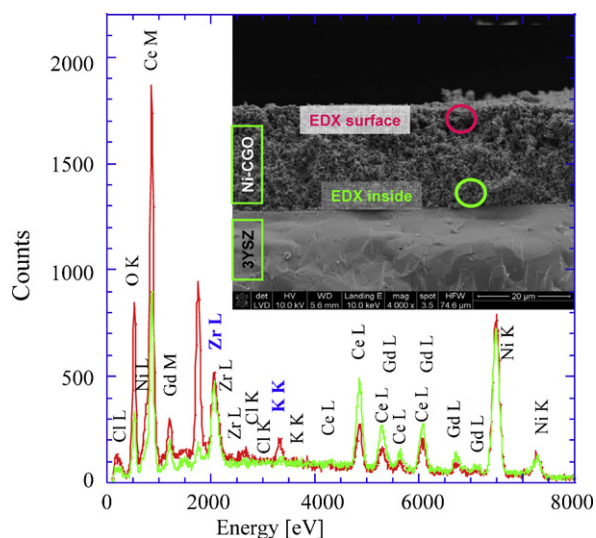
Fig. 9. EDX spectra collected from the fracture cross-section of the cell assembly exposed to low salt concentration. The red spectrum was collected from the near anode surface region, as indicated by the SEM micrograph inset, showing a clear peak at the energy for the potassium K emission line around 3400 eV and noticeable chlorine K and L emission lines at 2620 eV and 200 eV, respectively.

indicated in the SEM micrograph in Fig. 9, i.e. near the anode top surface (red spectrum) and near the anode–electrolyte interface. The EDX recorded near the top surface shows a clear fluorescence peak at the potassium K emission line (3313 eV) and noticeable chlorene K and L emission lines at 2620 eV and around 200 eV, respectively. There is no such peak in the EDX spectrum collected near the anode–electrolyte interface (green spectrum).

Higher concentrations of KCl in the anode were detected closer to the top surface, and lower concentrations in the anode range adjacent to the anode–electrolyte interface (Fig. 9). However, the amount of salt deposits on the anode surface and the porous structure after the long term test with low salt concentration were much lower than found in electrodes exposed to high salt concentrations. No delamination and cracking of anode structure were observed after the LSC test. However, cracking or delamination may always depend on the specific design, manufacture and operation of the cell. For example, in a 150 h cell operated in woodgas, cracks at the
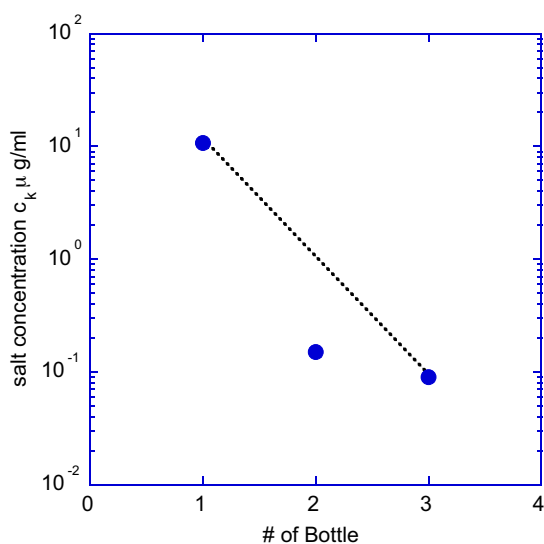
outer cell rim near oxidized nickel zones were observed after disassembly, but had apparently no serious negative impact on the overall operation of the SOFC [13].

4. Conclusions

Rapid structural degradation of a SOFC anode following forced salt deposition and condensation in pores might cover other effects and makes it impossible to study slower poisoning processes in porous anodes or electrolytes as anticipated under realistic operation conditions. A reactor system for simulating salt vapors of realistic gasified biomass fuelled system has therefore been developed. The particle sizes achieved in the vapor–aerosol KCl mixtures were in accordance with particle sizes detected in biomass gasified under realistic conditions. The salt concentration in the vapor–aerosol mixture was also comparable with concentrations known in real fuel mixtures produced by biomass gasifiers. We have in so far extended the range of equipment necessary to make realistic impurity studies for the degradation and long-term stability for biomass fuelled SOFC. In comparison with the reference test, the test with a low concentration of 6 ppm KCl showed a slight increase in the total area specific resistance from $1.99\,\Omega\,cm^2$ to $2.09\,\Omega\,cm^2$. The test with a high salt concentration of 3500 ppm KCl shows that the charge transfer resistance increased rapidly from $1.2\,\Omega\,cm^2$ to $3.6\,\Omega\,cm^2$ within 24 h of operation, accompanied by delamination effects on the anode and pore blocking by ice like deposits of KCl. The LSC test produced also small salt residuals on and in the anode, but EDX provided no evidence of K or Cl near the anode-electrolyte interface. Changes in the cermet microstructure were not identified in the LSC test. Future studies could for example address the question whether and how impurities accumulate in the SOFC components, and how the transient of accumulation can be met or simulated by forced failure using unrealistically high salt concentrations like the HSC test demonstrated in this work. Such tests should be extended towards other relevant impurities, such as Ca or Mg or P, for example.

Appendix A.

Two methods were applied to estimate the potassium (K) concentration in the gas stream. The total amount of K was calculated based on the K concentrations in each single gas washing bottles. The total amount of K in each bottle was added and divided by time and gas amount. The second method for evaluating the concentration and absorption coefficient of K in the water in gas washing bottles was by mathematical fitting of experimental data using a simple model:

$$c_1 = k\,c_{tot}$$
$$c_2 = k(c_{tot} - c_1)$$
$$c_3 = k(c_{tot} - c_2 - c_1)$$

where c_1, c_2 and c_3 are the concentrations of K of the first, second and third bottle, respectively. The coefficient k describes the salvation of the K vapor. c_{tot} is the concentration in the first bottle provided 100% of K were solved (maximum possible concentration). It is safe to assume that more than 95% KCl will actually be solved. The comparison between experimental (open symbols) and calculated (solid line, resembling an exponential fit) data in

Fig. 10. Experimental salt concentration (filled symbols) compared with anticipated ideal salt solution (dotted line with exponential decay) in the washing bottles.

Fig. 10 shows a remarkable deviation for the third bottle, which has the lowest salt concentration. According to this calculation, c_{tot} is 10.9 μg ml^{-1} and the absorption coefficient of K is approximately $k = 0.91$. The total amount of K collected in the bottles over 43 h was 2.725 mg, which corresponds to 6.9693×10^{-5} mol. During 2 min the amount of collected K was 2.7×10^{-8} mol. The amount of artificial wood gas passed through the system during 1 min was 100 ml, which is approximately 4.464×10^{-3} mol. The molar concentration of K and gas was 6.05 ppm.

References

[1] S. Baron, N. Brandon, A. Atkinson, B. Steele, R. Rudkin, J. Power Sources 126 (2004) 58–66.
[2] T. Horita, H. Kishimoto, K. Yamaji, M.E. Britoa, Y. Xiong, H. Yokokawa, Y. Hori, I. Miyachi, J. Power Sources 193 (2009) 194–198.
[3] K. Kohse-Höinghaus, P. Oßwald, T.A. Cool, T. Kasper, N. Hansen, F. Qi, C.K. Westbrook, P.R. Westmoreland, Angew. Chem., Int. Ed. 49 (21) (2010) 3572–3597.
[4] G.Y. Katsapov, A. Braun, Catal. Lett. 138 (3–4) (2010) 224–230.
[5] Y. Matsuzaki, I. Yasuda, Solid State Ionics 132 (2000) 261–269.
[6] Z. Cheng, S. Zha, M. Liu, J. Power Sources 172 (2007) 688–693.
[7] A. Lussier, S. Sofie, J. Dvorak, Y.U. Idzerda, Int. J. Hydrogen Energy 33 (2008) 3945–3951.
[8] A.J. Allen, J. Ilavsky, A. Braun, Adv. Eng. Mater. 11 (6) (2009) 495–501.
[9] A.J. Allen, J. Ilavsky, P.R. Jemian, A. Braun, J. Appl. Phys., to be submitted.
[10] C.M. Grgicak, R.G. Greene, J.B. Giorgi, J. Power Sources 179 (2008) 317–328.
[11] A. Braun, M. Janousch, J. Sfeir, J. Kiviaho, M. Noponen, F.E. Huggins, M.J. Smith, R. Steinberger-Wilckens, P. Holtappels, T. Graule, J. Power Sources 183 (2008) 564–570.
[12] P.V. Aravind, T. Woudstra, N. Woudstra, H. Spliethoff, J. Power Sources 190 (2009) 461–475.
[13] P. Hofmann, A. Schweiger, L. Fryda, K.D. Panopoulos, U. Hohenwarter, J.D. Bentzen, J.P. Ouweltjes, J. Ahrenfeldt, U. Henriksen, E. Kakaras, J. Power Sources 173 (2007) 357–366.
[14] F.N. Cayan, M. Zhi, S.R. Pakalapati, I. Celik, N. Wu, R. Gemmen, J. Power Sources 185 (2008) 595–602.
[15] J.P. Trembly, R.S. Gemmen, D.J. Bayless, J. Power Sources 163 (2007) 986–996.
[16] M. Zhi, X. Chen, H. Finklea, I. Celik, N.Q. Wu, J. Power Sources 183 (2008) 485–490.
[17] J.E. Bao, G.N. Krishnan, P. Jayaweera, J. Perez-Mariano, A. Sanjurjo, J. Power Sources 193 (2009) 607–616.
[18] K. Haga, S. Adachi, Y. Shiratori, K. Itoh, K. Sasaki, Solid State Ionics 179 (2008) 1427–1431.
[19] D.M. Keown, G. Favas, J. Hayashi, C. Li, Bioresour. Technol. 96 (2005) 1570–1577.
[20] E. Gustafsson, M. Strand, M. Sanati, Energy Fuels 21 (2007) 3660–3667.
[21] A. Norheim, D. Lindberg, J.E. Hustad, R. Backman, Energy Fuels 23 (2009) 920–925.
[22] A. Nordin, Biomass Bioenergy 6 (5) (1994) 339–347.
[23] K.-Q. Tran, K. IIsa, M. Hagström, B.-M. Steenari, O. Lindqvist, J.B.C. Pettersson, Fuel 83 (2004) 807–812.
[24] Y.P. Li, T.J. Wang, C.Z. Wu, Y. Gao, X.H. Zhang, C.G. Wang, M.Y. Ding, L.L. Ma, Ind. Eng. Chem. Res. 49 (2010) 3176–3183.
[25] P. Monkhouse, Prog. Energy Combust. Sci. 28 (2002) 331–381.
[26] K. Schofield, Proceedings of the ASME Turbo EXPO 2009 2 (2009) 993–1000.
[27] V. Haas, R. Birringer, H. Gleiter, S.E. Pratsinis, J. Aerosol Sci. 28 (1997) 1443–1453.
[28] K. Wegner, B. Walker, S.E. Pratsinis, J. Aerosol Sci. 31 (2000) 5214–5215.
[29] S. Panda, S.E. Pratsinis, Nanostruct. Mater. 5 (1995) 755–767.
[30] C. Ludwig, J. Wochele, U. Jörimann, Anal. Chem. 79 (2007) 2992–2996.
[31] C. Ludwig, A.J. Schuler, J. Wochele, S. Stucki, Water Sci. Technol. 42 (2000) 209–216.
[32] C. Ludwig, H. Lutz, J. Wochele, S. Stucki, Fresenius J. Anal. Chem. 371 (2001) 1057–1062.
[33] M. Gabra, E. Pettersson, R. Backman, B. Kjellström, Biomass Bioenergy 21 (2001) 371–380.